Implantable Fiber Bragg Grating sensor for continuous heart activity monitoring: ex-vivo and in-vivo validation

Davide Ferraro[1,2], Giacomo D'Alesio[1,2], Domenico Camboni[1,2], Ciro Zinno[1,2,3], Leone Costi[1,2,3], Max Haberbusch[4,5], Philipp Aigner[4,5], Martin Maw[4,5], Thomas Schlöglhofer[4,5], Ewald Unger[4], Andrea Aliperta[1,2], Fabio Bernini[6], Valentina Casieri[6], Domiziana Terlizzi[7], Guido Giudetti[1,2], Jacopo Carpaneto [1,2], Gianni Pedrizzetti[8], Silvestro Micera[1,2,9], Vincenzo Lionetti[6,7], Francesco Moscato[4,5,10], Luca Massari[1,2], Calogero Maria Oddo[1,2]

***Abstract*— Continuous and reliable cardiac function monitoring could improve medication adherence in patients at risk of heart failure. This work presents an innovative implantable Fiber Bragg Grating-based soft sensor designed to sense mechanical cardiac activity. The sensor was tested in an isolated beating ovine heart platform, with 3 different hearts operated in wide-ranging conditions. In order to investigate the sensor capability to track the ventricular beats in real-time, two causal algorithms were proposed for detecting the beats from sensor data and to discriminate artifacts. The first based on dynamic thresholds while the second is a hybrid convolutional and recurrent Neural Network. An error of 2.7 ± 0.7 beats per minute was achieved in tracking the heart rate. Finally, we have confirmed the sensor reliability in monitoring the heart activity of healthy adult minipig with an error systematically lower than 1 Bpm.**

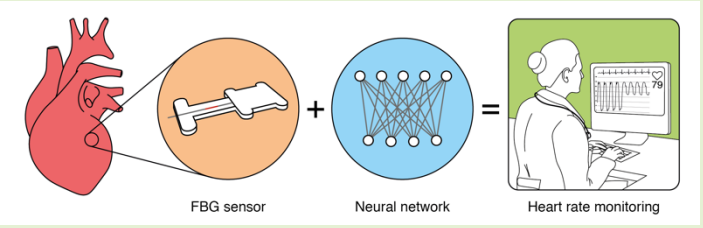

***Index Terms*—Fiber Bragg Grating, Heart monitoring, Neural Networks**

I. Introduction

Heart failure (HF) is a condition in which the heart is not able to pump enough blood to meet the needs of the body. It is a major health and economic challenge in both developing and developed countries [1]. Therefore, the continuous and reliable monitoring of cardiac activity remains a desirable foal in order to improve patient medication adherence, quality of medical care and to reduce costs due to outpatient visits and hospitalizations [2]. Its effectiveness has already been shown in chronic heart failure patients, whose hospitalizations can be reduced in a cost-effective manner [3], [4]. So far, continuous monitoring can provide a timely detection of major adverse cardiac events like malignant ventricular arrythmia [5] or myocardial infarction [6], which would improve clinical outcomes [7].

A. Heart activity monitoring

One of the main physiological parameters used to assess the heart status is the ventricular beat or contraction frequency, defined as heart rate. It represents a mechanism for regulating cardiac output and its value should fall in an appropriate range, outside of which further evaluation could be needed in order to assess the need of therapeutic intervention [8]. Nevertheless, its patterns can reveal more information, for example, its acceleration can be used to predict ventricular tachyarrhythmia [9], its abnormal recovery after exercise is correlated to coronary artery disease [10], and the sequence of R-R interval values used to detect atrial fibrillation [11].

Heart rate variability has been gaining an increased attention for its relationship with the autonomic nervous system and its prognostic value in a plethora of heart disease signs. It can be used to predict ventricular arrhythmias [12], [13] or the risk of heart decompensation days before hospital admission [14].

These parameters can be measured in a non-invasive manner,

This study was supported by the European Commission through the H2020-FETPROACT-2018-01 NeuHeart Project (Grant Agreement 824071). This study was also supported in part by the Austrian Research Promotion Agency (FFG) through the R&D Infrastructure Project M3dRES (nr. 858060).

[1] The BioRobotics Institute, Scuola Superiore Sant'Anna, Pisa, Italy;
[2] Department of Excellence in Robotics & AI, Scuola Superiore Sant'Anna, Pisa, Italy;
[3] Department of Information Engineering, University of Pisa, Pisa, Italy;
[4] Center for Medical Physics and Biomedical Engineering, Medical University of Vienna, Vienna, Austria;
[5] Ludwig Boltzmann Institute for Cardiovascular Research, Vienna, Austria;
[6] Institute of Life Sciences, Scuola Superiore Sant'Anna, Pisa, Italy;
[7] UOS Anesthesiology and Intensive Care Medicine, Fondazione Toscana Gabriele Monasterio per la Ricerca Medica e di Sanita Pubblica, Pisa, Italy;
[8] Department of Engineering and Architecture, University of Trieste, Trieste, Italy;
[9] Translational Neural Engineering Laboratory, Center for Neuroprosthetics and Institute of Bioengineering, EPFL, Lausanne, Switzerland;
[10] Austrian Cluster for Tissue Regeneration, Vienna, Austria.

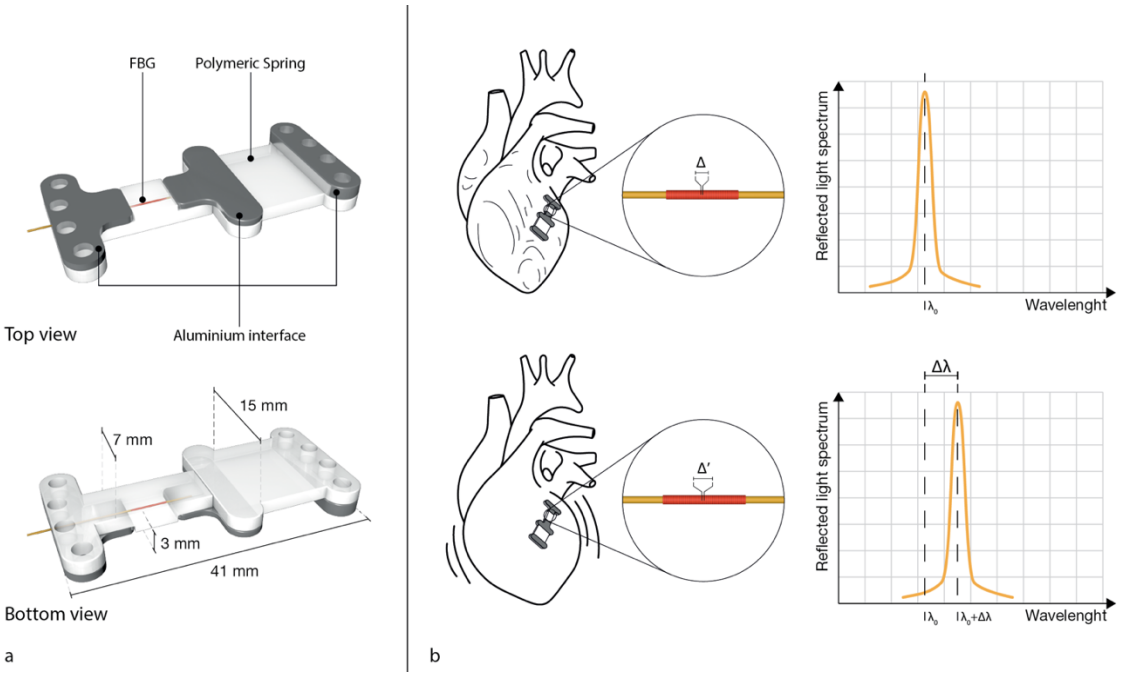

Fig. 1. a) top and bottom view of the realized sensor. b) FBG working principle applied to this case study: when the heart is contracted (above) the sensor is in a resting position and the peak wavelength of the reflected light spectrum at its minimum; after heart expansion (below) the sensor is stretched, thus the peak wavelength increases.

by means of electrodes, stethoscopes or LEDs placed on the skin surface — respectively used in electrocardiogram (ECG), phonocardiogram (PCG) and photoplethysmogram (PPG) monitors. ECG detects heart electrical activity, and it is commonly used to evaluate the heart rhythm. PCG detects heart sounds and has high potential to detect valvular and important cardiovascular diseases. PPG measures the blood volume variation in blood vessels, therefore providing less information about the heart. These systems are affected by different artifacts due to movements and other kind of physical interferences, such as electrical or from ambient light. Moreover, in the case of non-invasive ECG, the electrodes are not suitable for long-term continuous use [15].

While non-invasive solutions are useful for monitoring the healthy population, implantable systems can be mandatory in patients who are more exposed to adverse events in the long-term out-of-hospital care, like those undergoing cardiac surgery or heart transplantation [16], [17]. Invasive solutions to track cardiac function [18], [19], like the one we propose in this study, can be more accurate and effective in detecting pathological changes and assessing the progression of diseases thanks to their direct access to left ventricular wall. As an example, this advantage can be seen in implantable hemodynamic monitors in heart failure patients, whose impending hospitalization can be predicted weeks before by measuring increasing filling pressures [4]. Invasive ECG measurement can provide a long-term continuous monitoring, but the electrical activity is only indirectly coupled to mechanical one. Indeed, in some circumstances ECG may not refer to the cardiac mechanical function such as in electromechanical dissociation leading to cardiac arrest [20].

B. Heart strain sensing

The usage of ventricular strain from magnetic resonance and ultrasound imaging is a very active area of research in the field of cardiovascular translational medicine [21], [22]. The strain depends on many variables in the cardiovascular system. For example, myocardial contractile force and excitation-contraction coupling, or the hemodynamic preload and systemic vascular resistance (afterload). The strain rate can be used as a measure of cardiac contractility. Both can change in a plethora of diseases, which highlights the tight link to the cardiovascular system health. For example, reduced strain combined to higher myocardial stiffness is a hallmark of cardiomyopathy development towards heart failure [23], and it is a predictor of major cardiac adverse events leading to disability and mortality in an hospital setting [24].

The previously mentioned imaging systems are unwieldy and bound to the time of an operator-driven investigation, thus they are confined to a hospital setting. In contrast, an implantable, soft, miniaturized and sensitive strain sensing device would allow longer monitoring of the abovementioned parameters in every-day settings in order to detect the onset of major cardiac adverse events even at home. Moreover, it could provide a real-time monitoring of the cardiac response to medications in order to develop a personalized therapy.

C. Objectives of the study and structure of the manuscript

In this study we present a soft implantable strain sensor, together with two complementary algorithms to track the heart rate, with the objective of monitoring the heart by means of continuous and reliable data on its mechanical activity. Our sensor uses a Fiber Bragg Grating (FBG) transducer to measure

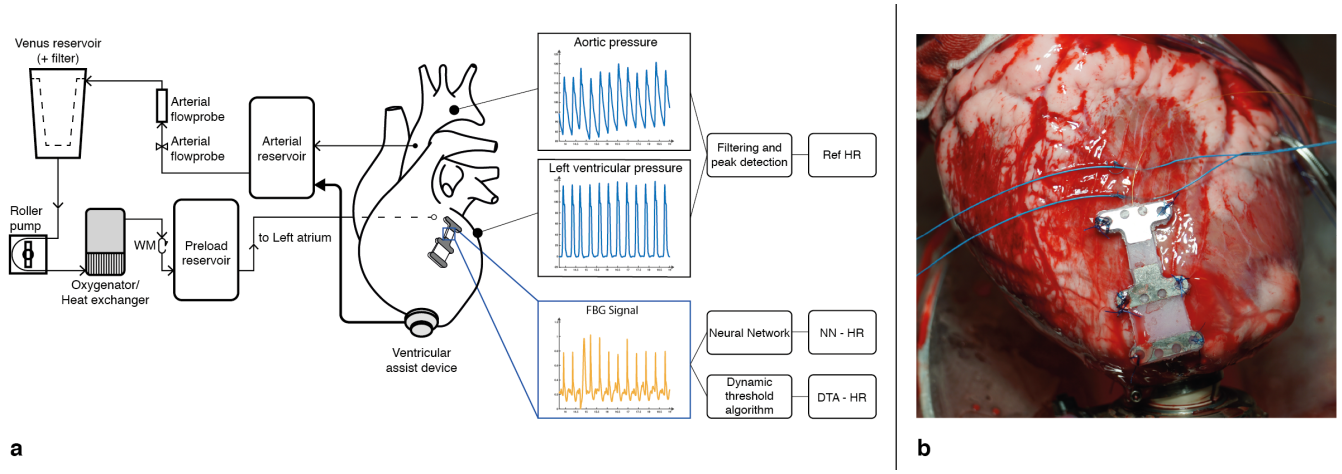

Fig. 2. a) Left part: setup for isolated heart activity support and control (WM: working mode clamp). Right part: extracted variables and processing needed to compute the heart rate (HR). b) Image of the isolated heart setup.

the strain of the ventricular region onto which it is attached. While the mentioned imaging techniques give us a global overview of the heart deformation pattern, but struggle in time and spatial sensitivity, FBG strain sensing offers excellent temporal resolution, spatial acuity and measurement accuracy [25], [26]. We test our sensor in an isolated ovine heart setup, under wide-ranging conditions, and in anesthetized minipig.

In section II.A, the sensor design and its working principle are presented. Then, the experimental setup and the processing of the gathered data are described in section II.B. In section II.C, we propose an algorithm based on dynamic thresholds and a neural network to detect the beats from sensor data. The validation procedure is discussed in section II.D and II.E. The in-vivo testing setup is described in section II.F.

The results of both the algorithms, on both ex- and in-vivo data are presented and discussed in section III. Finally, section IV presents the conclusion and next steps.

II. Materials and Methods

A. Working principle and sensing device

The developed sensor consists of an optical fiber housing one single FBG grating (FEMTOPlus Grating; FemtoFiberTec GmbH, Berlin, Germany) embedded into a soft material (Dragon Skin 30, Smooth-on, USA). The sensor is composed of two elastic in-series elements divided by three rigid aluminum parts (Fig. 1). The sensor is intended to be sutured to the epicardial surface of the left ventricle (LV), through the holes within the metallic parts. In order to ensure proper mechanical stability, the sensor could be anchored in at least two different points.

The broader elastic part acts as a spring absorbing most of the strain and therefore avoiding damage to the fiber. The thinner polymer part encapsulates the optical fiber, it is responsible to transmit the strain to the sensing element (FBG) and to limit its bending which could be harmful if excessive. Two glues were used to bond the elements of the sensors: i) Sil-poxy (Smooth-on, USA) to glue the polymer to the metallic parts and ii) UV glue (Loctite, USA) for bonding the optical fiber with the metal plates. The realized sensor has an overall length of 41 mm, 3 mm thickness and a width of 7 mm and 15 mm for the thin and broad polymers part, respectively. The embedded optical fiber was laterally centered in the middle of the thin polymer part and was aligned with the longitudinal axis.

An FBG is a micro resonant structure that reflects a defined wavelength, the so-called Bragg wavelength λ_B, when a broadband light source is fed through the optical fiber. The specific wavelength that is reflected-back is described by the grating period (Δ_B) and the effective refraction index (η_{eff}) as highlighted in (1):

$$\lambda_B = 2\,\eta_{eff}\,\Delta_B \quad (1)$$

Strain suffered by the optical fiber leads to variation of λ_B. In the sensor, we embedded a grating that has a length of 5 mm, an unstrained Bragg wavelength of either 1565 nm or 1545 nm and a strain sensitivity of 1.21 pm/με. The sensor was sutured onto the epicardium wall to measure the heart rate by tracking the λ_B of the FBG grating. Fig. 1 explains the FBG transduction principle applied to our case study. During the cardiac cycle, all the heart chambers are involved in a contraction phase (systole) and a relaxion phase (diastole). During this transition, the heart elongates the attached sensor, thus passing from an unstrained condition (systole) to a strained condition (diastole). Systole and diastole represent, respectively, the cases with maximum and minimum heart deformation and hence maximum and minimum wavelength shift of the λ_B.

The fiber is plug into an optical interrogator which reads the reflected light spectrum and extracts the peak wavelength.

B. Experimental setup and data collection

The experimental setup, shown in Fig. 2, consists of the isolated heart, the devices needed to operate it, the probes needed to extract the heart cycle data, the interrogator and the FBG sensor, which is sutured on the inferior lateral wall of the LV, considered to be an area of high strain.

Three sheep hearts were harvested similar to cardiac transplantation with administration of cardioplegia and ice cooling in the operating room. The hearts were then connected to the isolated heart apparatus and a Ventricular Assist Device (VAD) (HVAD, Medtronic Inc.) implanted at the ventricular apex. Using first the Langendorff perfusion, the hearts were rewarmed and restarted beating. Then using a working-heart mode (i.e. the heart operates as in the in-vivo setting) different

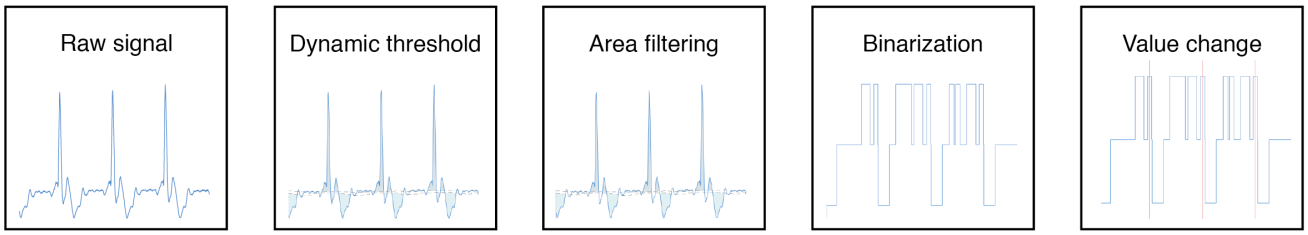

Fig. 3. Graphical illustration of the processing step of the Dynamic Thresholds algorithm.

hemodynamic conditions were investigated [27].

Ventricular Assist Device pump speed, pacing, cardiac output, preload and adrenergic stimulation were gradually varied across the ranges indicated in TABLE I, each one in an independent experiment where only one variable was controlled, thus obtaining a consistent amount of data (around 95 minutes, sampled at 200 Hz for a total of 1.14 million individual samples).

TABLE I
VARIABLES CONTROLLED IN INDIVIDUAL EXPERIMENTS.

Controlled variable	*Explored ranges*
Pacing	80-180 Bpm (slow and fast rate of change)
Left Atrial Pressure (Preload)	3-13 mmHg
VAD pump speed	2400-3200 Rpm
Cardiac Output	1-5 l/m
Adrenergic stimulation	0.5-1ml Dobutamine, 0.2-2.5mg Epinephrine

The heart phases used for reference were computed by processing the left ventricular and aortic pressure. In order to extract the peaks of the ventricular pressure, the baseline was removed by subtracting the mobile median, and a lowpass Butterworth filter (second order with cut-off frequency of 2.5 Hz) was applied. Small ventricular contractions which did not lead to an aortic pressure increase were removed. Finally, for each remaining peak of the ventricular pressure, the time segmentation of each systole was computed by finding the maximum and minimum of the first derivative. Thereby obtained reference peaks were used to evaluate the performance of the algorithms (Fig. 2, right part of panel a), and the systole segmentation was used as ground-truth for training a Neural Network (NN).

The interrogator (SmartScan; Smart Fibres Ltd, Bracknell, UK) reads the reflected peak wavelength with a resolution < 1 pm. The peak wavelength tracking is operated directly by the FBG interrogator, whereas the unstrained peak wavelength is subtracted from the sensor output to obtain the peak wavelength change.

C. Heart beats extraction algorithms

The sensor capability of monitoring the heart rate was validated in an isolated sheep heart by means of: i) a dynamic thresholds (DT) algorithm and ii) a NN. Both algorithms receive the peak wavelength change, output the times at which the beats occur and are meant to work in an online setting.

1) *Dynamic Thresholds algorithm*

The DT algorithm is lightweight, easy to implement and its parameters are not learned but calibrated with pilot trials. Fig. 3 displays how the DT algorithm operates. This algorithm uses a 2 s time window, updated every 100 ms, to dynamically compute the 0.4 and 0.6 quantiles of the signal. These values are used as thresholds to segment the heart cycle into peak, median and trough areas. The trough areas shorter than 120 ms and peak areas shorter than 50 ms are removed. Finally, a beat is counted when the passage from a peak to a trough area is detected. Its timestamp is the center of the last peak area.

2) *Neural Network architecture*

The NN is a Temporal Convolution Network (TCN) [28] followed by a Long Short-Term Memory (LSTM) [29] layer which features a total of 66k weights. There are 6 residual

TABLE II
NEURAL NETWORK STRUCTURE.

Layer	*Kernel size*	*Dilation*	*Output Channels*	*Under-sampling*	*Activation*
Input			1	1x	
TCN Block 1	6	1	24*	1x	ReLU
TCN Block 2	6	4	24	1x	ReLU
Max pooling	4		24	4x	
TCN Block 3	4	1	34*	4x	ReLU
TCN Block 4	4	2	34	4x	ReLU
Max pooling	2		34	8x	
TCN Block 5	2	1	48*	8x	ReLU
TCN Block 6	2	2	48	8x	ReLU
Max pooling	2		48	16x	
LSTM			48	16x	Tanh
Layer normalization			48	16x	
1D Convolution	1	1	1	16x	Sigmoid

*the skip connection features a matching convolution, since there is a change in the number of channels

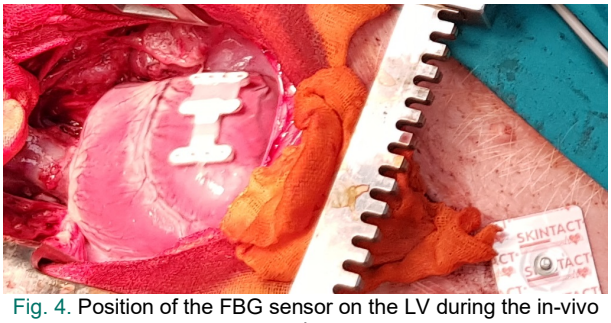

Fig. 4. Position of the FBG sensor on the LV during the in-vivo experiment.

blocks with a Max Pooling operation every two blocks. Each residual block is composed of two consecutive 1D causal dilated convolutions with ReLU activation, (i.e., their output depends only on previous time values and the inputs are spaced to increase the receptive field). In the residual blocks the output is obtained by summing the result of the last convolution directly to the block input. In case they have a different number of channels a lightweight channel-wise dense layer (i.e., a convolution with kernel size equal to one) is used to match them. Finally, an LSTM layer with layer normalization produces an embedding of 48 values every 16 timesteps and the network output is computed with a channel-wise dense layer with sigmoid activation. TABLE II shows the exact parameters used in each block and the progressive under-sampling due to max pooling. Each TCN block aggregates information from a number of timesteps equal to the kernel size times the dilation.

The NN target is the systole mask (1 when the heart is in systole phase, 0 otherwise) which changes its value at the very start of pressure increase. The loss used is binary cross-entropy for each timestep. The large convolution kernels, the dilations and the max pooling grant the aggregation of information from a wide receptive field of almost 0.5 s. Even if there is no long-term dependence between the signal and the output, an LSTM was used because of its dynamic expressiveness [30], which is useful to a task like this in which the network learns to switch state at the systole boundaries. The network is trained with stochastic gradient descent with 0.9 Nesterov momentum and a 0.005 learning rate with cosine decay schedule and restarts (with alpha equal to 0 and 50 decay steps, multiplied by 2 at each restart). Input sequences of 15 s duration are grouped with batch size of 15 and used as training inputs. Furthermore, data augmentation is performed by extracting them dynamically at random positions from longer continuous sequences of training data. The NN does not directly outputs the individual beats, but a time series of value between 0 and 1. First, a centered mobile mean filter with window width equal to 3 is used to smoothen the output. A beat is detected every time the unfiltered output is above a 0.5 threshold and a peak above 0.5 follows in the smoothed one. The computation time of a single output is estimated on an Intel i5 10th-gen processor running at 3.3GHz with 16GB RAM, disabling parallelism to employ only one core. The evaluation is run on a long sequence and the total time is divided by the number of outputs. Finally, the computation time results are averaged over 100 trials.

D. Heart rate (HR) error computation

Once the beat timing is obtained, an HR value is retrieved for each second of the signal by using the mean beat interval in a 6 s window. Sampling at fixed intervals and making the HR smoother allows for a better one to one comparison. Since the HR is the reciprocal of the time interval between two detected beats, its value can be very sensitive to small positioning errors, i.e., its error distribution tends to have a heavy tail. For this reason, the mean absolute error (MAE) was computed, having a sensitivity to outliers halfway between the root mean square error and the median absolute error. The network under-sampling introduces a baseline error due to the inability to precisely express the beat timing (an expected error even with perfect beat detection). The HR filtering window width decreases the effect of such an error but a trade-off should be operated in order to dynamically track increasing or decreasing HR. We studied the optimal balance by using simulations on real data to assess the under-sampling baseline error and simulation on HR ramps to assess the following error. We found a 6 s width to be a good trade-off, with an expected 0.75 Bpm error due to temporal discretization.

E. Performance validation methods for heart beats extraction algorithms

During data collection the isolated heart was stressed beyond normal working conditions. To fairly assess the algorithms performance, we split the dataset into normal and high heart rate variability (HRV) sequences. The HRV was measured with the root mean square of successive RR interval differences (RMSSD) and a value of 130 ms has been selected as a threshold for splitting data (values up to 1000 ms were measured). The resulting normal and high variability datasets contain respectively 60% and 40% of data, approximately.
Moreover, the expected error and the variation (mean absolute deviation) was computed with 10-fold cross validation, both for the NN and for the DT algorithm – which does not learn based on data, but was tested in the same manner for comparison. In order to perform early stop, before each NN training a validation fold, separate from test fold, was extracted from training data.

F. In-vivo validation

To further assess the proposed sensor and algorithms, an in-vivo experiment with a porcine heart was performed. An adult male mini-pig (40kg body weight) was anesthetized (isoflurane 1.0-1.5%) and mechanically ventilated under monitoring of vital parameters in accord with previous study [18]. Body temperature was maintained at 36.5°–39°C. The left femoral artery was surgically exposed, cannulated and connected to a P23ID strain-gauge transducer to allow continuous measurement of the arterial blood pressure. A median sternotomy was performed to open the chest and the beating heart was exposed after anterior pericardiectomy. The FBG sensor was sutured to the epicardium of the mid-anterior region of the left ventricular wall by two stitches (Prolene 6-0). The direction of the optical fiber was approximately parallel to the long axis of the ventricle. Fig. 4 shows the sensor position during the experiment.

As a reference, physiological parameters like respiratory rate, heart rate, and cardiac rhythm were monitored. Moreover, hemodynamic signals were recorded on an eight-channel Gould polygraph recorder (model 5900; Gould Inc., Cleveland, OH, USA). The signals were recorded through an analog-digital

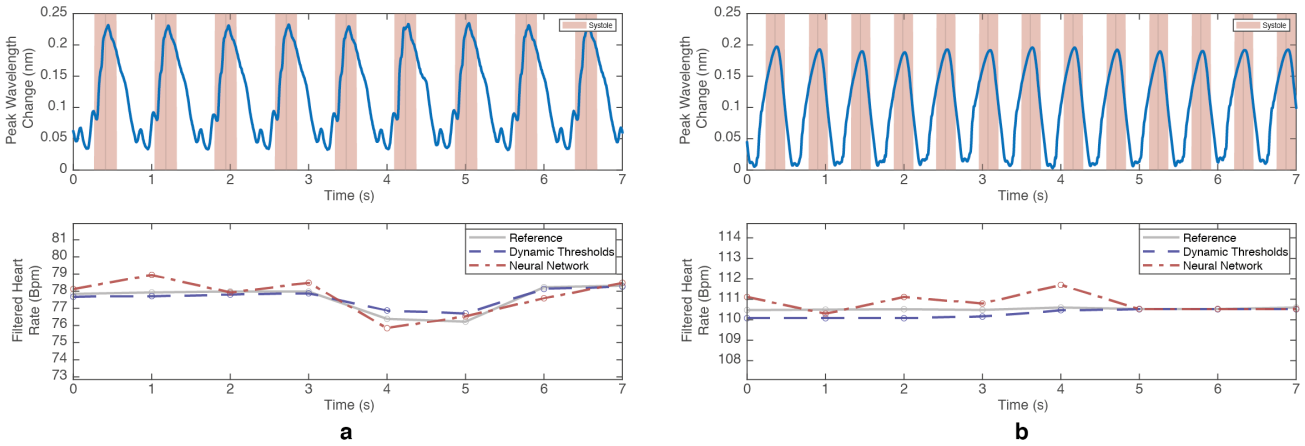

Fig. 5. Examples of sensor output with the reference systole mask (above) and the corresponding filtered heart rates (below) from a) the isolated heart setup and b) the in-vivo setup.

converter (AD Instruments). Mean femoral artery blood pressure was measured because it reliably reproduces central aortic pressure during cardiac surgery [31]. Pulse pressure is a widely used as surrogate of stroke volume in hospital setting and it was computed as the difference between systolic and diastolic arterial pressure [32]. Cardiac output was estimated on a Windkessel model, it was calculated as the product of pulse pressure and heart rate, divided by 1000 [33]. Systemic vascular resistance was calculated as the ratio between mean arterial pressure and cardiac output, multiplied by a correction factor of 79.9 [34]. Finally, rate pressure product was calculated as the product of systolic arterial pressure and heart rate. It is a reliable indirect index of myocardial oxygen consumption during general anesthesia and cardiac surgery [35].

In-vivo FBG data were acquired through an optical interrogator (FBG-Scan 904; FBGS, Geel, BE) with a 10 pm resolution over a 5 minutes period. Leveraging on the same algorithms (i.e., DT and NN), without any further training on this data, we explored the capabilities of the sensor to properly measure the heart rate of the animal.

III. Results and Discussion

Within this work, we presented a soft sensor embedding one FBG and tested its capability in tracking the heart activity in real time by ex-vivo and in-vivo studies in large mammals.

To have a well-rounded assessment of the sensor capabilities, the isolated hearts were stressed in wide-ranging conditions reflecting realistic physio-pathologic conditions. In particular, the obtained samples display normal and high heart rate variability, this latter due to increased arrhythmic activity.

A sample from the dataset and the relative reference and output heart rates can be seen in Fig. 5a, also displaying the correlation between the heart phase (systole in red) and the sensor response. Fig. 5b shows a sample of in-vivo data. TABLE III compares the obtained results on normal, high variability data and on the whole dataset. TABLE IV sums up the error distribution, which can be fully evaluated in Fig. 6, showing the Bland-Altman plots of the two algorithms on the whole dataset.

TABLE III
Comparison of the results of the two algorithms on the whole dataset and its subsets.

Heart rate MAE [Bpm]	*Normal variability*	*High variability*	*All dataset*
Dynamic Thresholds	9.9 ± 2.4	12.9 ± 4.6	11.2 ± 2.5
Neural Network	2.7 ± 0.7	4.6 ± 1.2	3.4 ± 0.7

TABLE IV
Maximum absolute heart rate error in dataset subsets.

Dataset percentage	*Dynamic Thresholds*	*Neural Network*
50%	< 1 Bpm	< 1 Bpm
66%	< 5 Bpm	< 1.6 Bpm
83%	< 22 Bpm	< 5 Bpm

The DT algorithm accurately detects the HR in two thirds of the dataset, as shown in TABLE IV. Though, since its parameters are fixed and the algorithm does not adapt itself on data, it fails to display the same accuracy when the isolated hearts are put in severe stress condition. Indeed, Fig. 6a, referring to DT algorithm, shows an error bias and a heavy tail.

On the contrary, the NN features a more balanced, less biased error, beside a higher overall accuracy, which can be seen in Fig. 6b. It should however be noted that the computational workload is much higher with the neural network than with the dynamic thresholds algorithm: 7.3 MFLOPs vs 50 kFLOPs, approximately, resulting in a two order of magnitudes difference. Despite this, we estimated the computation time of a single NN output on an Intel i5 CPU core to be 0.07 ms ± 0.01 ms out of an 80 ms interval between consecutive outputs. As a consequence, we can assert that real-time deployment on the edge of both the DT and the NN algorithms is feasible. Moreover, dedicated hardware such as FPGA accelerators have been reported to achieve sub-ms execution of recurrent NNs with a bigger computational footprint than ours [36].

We also report the cross-validated accuracy, recall and precision on the test folds, respectively: 93.3% ± 1.0%, 93.2% ± 0.9% and 93.3% ± 1.3%. These metrics are computed on the raw output mask and indicate a successful NN training. Due to the under-sampling and the way the target is used to train the NN, the timing of the predicted beats is not as precise as the data would allow. When computing the HR, we still have a precise estimation since we use multiple beats; though, this hinders the

potential to accurately measure indicators like the HRV. This problem could be solved by adapting methods from the field of object detection and image segmentation, e.g., Yolo [37] or Unet [38]. Still, our approach, which uses an LSTM and a simple post-processing strategy, allows an easy-to-train NN for real-time detection of the beats.

The in-vivo experiment features a healthy heart of a hemodynamically stable anesthetized minipig. Both algorithms (tuned in the isolated heart setting) show excellent transfer capability to the in-vivo setting and perform with error close to zero, 0.1 Bpm and 0.6 Bpm for DT and NN, respectively. The hemodynamic values measured during the experiment show a healthy minipig heart and suggest that our soft sensor does not interfere with heart dynamics (TABLE V).

TABLE V
HEMODYNAMIC VALUES MEASURED AND CALCULATED DURING ASSESSMENT OF FBG-BASED SENSOR IN ANESTHETIZED MINIPIG AT 1, 3 AND 5 MINUTES.

Variable	*1 minute*	*3 minutes*	*5 minutes*
Heart Rate (Bpm)	108	110	108
Systolic Pressure (mmHg)	83	81	80
Diastolic Pressure (mmHg)	52	50	51
Mean Arterial Pressure (mmHg)	62.3	60.3	60.7
Pulse Pressure (mmHg)	31	31	29
Cardiac Output (L/min)	3.35	3.41	3.13
Systemic Vascular Resistance (dyn-s/cm^5)	1487	1413	1549
Rate Pressure Product	8964	8910	8640

IV. CONCLUSION AND FUTURE PERSPECTIVES

We demonstrated that the presented strain sensor has a strongly versatile ability to detect the frequency of the heart beats resulting from proper cardiac electro-mechanical coupling. We proposed two algorithms to this aim: the DT algorithm which is lightweight but less effective in challenging conditions; and the accurate, robust, but computationally heavier NN. We envision a usage in embedded settings in which they complement each other. Given the relationship between strain and several cardiovascular diseases, we believe our sensor has the potential to advance the state of the art in heart monitoring, allowing to detect more promptly the dysfunctions arising in patients with severe conditions at risk of adverse cardiac events.

Future work will be aimed at reducing the sensor invasiveness by means of a smaller size, using a biocompatible polymer, optimized shapes and simpler standardized positioning procedures. Moreover, although our goal is to avoid reactive materials, we cannot exclude fibrotic response at the implantation site as already observed in humans receiving pacemaker and defibrillator leads or heart valve prostheses. Anti-fibrotic coatings of surfaces may be used in future chronic applications to reduce the risk of a fibrotic response, which varies with the individual and may affect the sensitivity of the sensor. These progresses will be followed-up by a study dedicated to the long-term influence of the device presence on the tissues nearby. In addition to that, an imaging-based simulation method could be developed to identify the optimal positioning and direction of the sensor onto the ventricle according to the specific heart condition. We will also continue assessing the sensor capabilities by gathering in-vivo data related to pathological conditions and employ it with the aim of measuring additional clinically relevant variables, like heart rate variability, other strain-derived parameters and myocardial stiffness. Additionally, our sensor can measure the cardiac electro-mechanical coupling, when coupled to ECG.

Our sensor includes a single sensing element, but the FBG technology allows the use of multiple gratings inside a single sensor fiber, leveraging on wavelength multiplexing capabilities [39]. Implementing such a feature would grant the ability to sense the strain in multiple locations without additional wiring encumbrance, which can be a crucial aspect in such scenarios [40]. Moreover, in the present study temperature was not varied within each experimental session, however temperature changes should be rejected in the perspective of future chronic use: possible solutions include filtering operations, since mechanical and thermal effects have different characteristic timing, and the integration of an additional dummy FBG positioned so to be sensitive to temperature changes but not to myocardial strain.

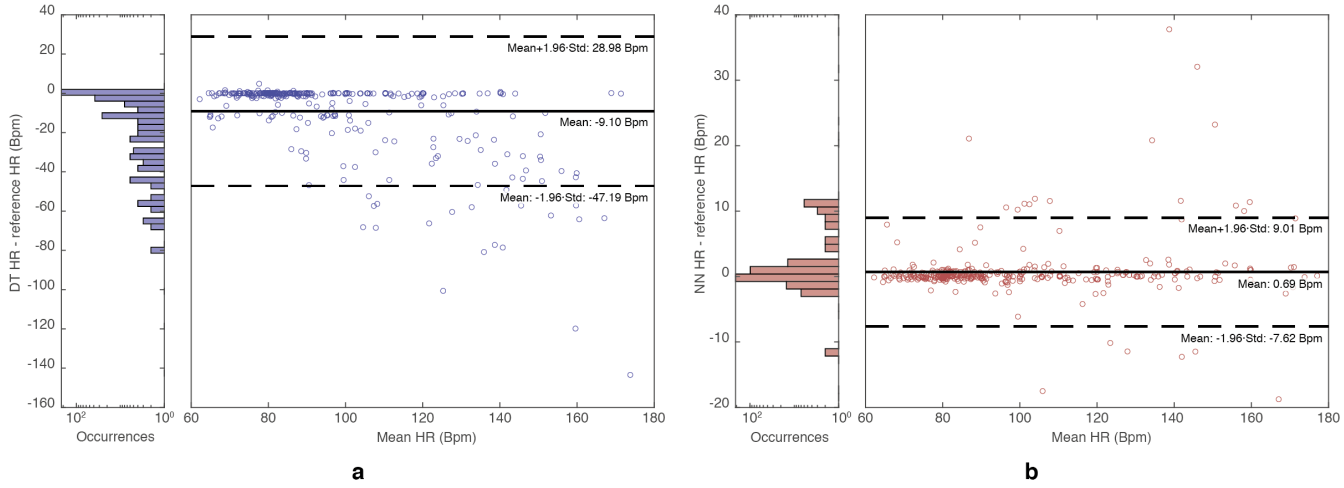

Fig. 6. Bland-Altman plots of the filtered HR measurement error of a) the DT algorithm and b) the NN on the whole dataset. On the side the error distribution is shown. For a clear visualization, only the mean of the errors of each 15 seconds-long test sample is displayed.

Both the isolated heart and the in-vivo animal experimental setups allowed to successfully use a wired external photonic interrogator . Our aim, indeed, was to perform an acute testing of the feasibility of the developed sensor to monitor the heart biomechanical activity. Acute testing does not strictly require wireless communication, and transcutaneous links may be successfully used also in experimental trials lasting some months [41]. However, to have implantable telemetry electronics will be fundamental in order to achieve chronic implants applied clinically. The long term roadmap includes the future integration of our sensor inside a fully implanted device. FBGs are soft, flexible, compatible with magnetic resonance imaging [42] and have minimal power requirements. The main challenge thus remains the bulkiness of state of the art commercial interrogators: this is part of the long term strategy of this project, and miniaturized solutions for FBG interrogators are nowadays emerging both commercially and in research studies [43], [44].

REFERENCES

[1] A. Groenewegen, F. H. Rutten, A. Mosterd, and A. W. Hoes, “Epidemiology of heart failure,” *Eur. J. Heart Fail.*, vol. 22, no. 8, pp. 1342–1356, 2020, doi: 10.1002/ejhf.1858.

[2] T. M. Ruppar, P. S. Cooper, D. R. Mehr, J. M. Delgado, and J. M. Dunbar-Jacob, “Medication adherence interventions improve heart failure mortality and readmission rates: Systematic review and meta-analysis of controlled trials,” *J. Am. Heart Assoc.*, 2016, doi: 10.1161/JAHA.115.002606.

[3] R. A. Clark, S. C. Inglis, F. A. McAlister, J. G. F. Cleland, and S. Stewart, “Telemonitoring or structured telephone support programmes for patients with chronic heart failure: Systematic review and meta-analysis,” *Br. Med. J.*, 2007, doi: 10.1136/bmj.39156.536968.55.

[4] J. F. Veenis and J. J. Brugts, “Remote monitoring of chronic heart failure patients: invasive versus non-invasive tools for optimising patient management,” *Netherlands Heart Journal*. 2020, doi: 10.1007/s12471-019-01342-8.

[5] S. Mandala, T. Cai Di, M. S. Sunar, and Adiwijaya, “ECG-based prediction algorithm for imminent malignant ventricular arrhythmias using decision tree,” *PLoS One*, 2020, doi: 10.1371/journal.pone.0231635.

[6] U. R. Acharya, H. Fujita, S. L. Oh, Y. Hagiwara, J. H. Tan, and M. Adam, “Application of deep convolutional neural network for automated detection of myocardial infarction using ECG signals,” *Inf. Sci. (Ny).*, 2017, doi: 10.1016/j.ins.2017.06.027.

[7] L. Lambert, K. Brown, E. Segal, J. Brophy, J. Rodes-Cabau, and P. Bogaty, “Association between timeliness of reperfusion therapy and clinical outcomes in ST-elevation myocardial infarction,” *JAMA - J. Am. Med. Assoc.*, 2010, doi: 10.1001/jama.2010.712.

[8] S. A. Magder, “The ups and downs of heart rate,” *Crit. Care Med.*, 2012, doi: 10.1097/CCM.0b013e318232e50c.

[9] T. Thong and M. H. Raitt, “Predicting imminent episodes of ventricular tachyarrhythmia using heart rate,” *PACE - Pacing Clin. Electrophysiol.*, 2007, doi: 10.1111/j.1540-8159.2007.00775.x.

[10] S. Ghaffari, B. Kazemi, and P. Aliakbarzadeh, “Abnormal heart rate recovery after exercise predicts coronary artery disease severity,” *Cardiol. J.*, 2011.

[11] O. Faust, A. Shenfield, M. Kareem, T. R. San, H. Fujita, and U. R. Acharya, “Automated detection of atrial fibrillation using long short-term memory network with RR interval signals,” *Comput. Biol. Med.*, 2018, doi: 10.1016/j.compbiomed.2018.07.001.

[12] M. J. Reed, C. E. Robertson, and P. S. Addison, “Heart rate variability measurements and the prediction of ventricular arrhythmias,” *QJM - Monthly Journal of the Association of Physicians*. 2005, doi: 10.1093/qjmed/hci018.

[13] W. Grimm, I. Herzum, H. H. Müller, and M. Christ, “Value of heart rate variability to predict ventricular arrhythmias in recipients of prophylactic defibrillators with idiopathic dilated cardiomyopathy,” in *PACE - Pacing and Clinical Electrophysiology*, 2003, doi: 10.1046/j.1460-9592.2003.00060.x.

[14] P. B. Adamson *et al.*, “Continuous autonomic assessment in patients with symptomatic heart failure: Prognostic value of heart rate variability measured by an implanted cardiac resynchronization device,” *Circulation*, 2004, doi: 10.1161/01.CIR.0000139841.42454.78.

[15] P. K. Jain and A. K. Tiwari, “Heart monitoring systems-A review,” *Comput. Biol. Med.*, 2014, doi: 10.1016/j.compbiomed.2014.08.014.

[16] V. Lionetti and L. Barile, “Perioperative cardioprotection: back to bedside.,” *Minerva Anestesiol.*, vol. 86, no. 4, pp. 445–454, Apr. 2020, doi: 10.23736/S0375-9393.19.13848-5.

[17] A. B. Shah, J. K. Patel, M. Rafiei, R. P. Morrissey, M. M. Kittleson, and J. A. Kobashigawa, “The impact of mean first-year heart rate on outcomes after heart transplantation: Does it make a difference?,” *Clin. Transplant.*, 2013, doi: 10.1111/ctr.12188.

[18] V. Lionetti *et al.*, “Impact of acute changes of left ventricular contractility on the transvalvular impedance: validation study by pressure-volume loop analysis in healthy pigs.,” *PLoS One*, vol. 8, no. 11, p. e80591, 2013, doi: 10.1371/journal.pone.0080591.

[19] V. Gemignani *et al.*, “Transthoracic Sensor for Noninvasive Assessment of Left Ventricular Contractility: Validation in A Minipig Model of Chronic Heart Failure,” *Pacing Clin. Electrophysiol.*, vol. 33, no. 7, pp. 795–803, Jul. 2010, doi: 10.1111/j.1540-8159.2009.02684.x.

[20] C. Mehta and W. Brady, “Pulseless electrical activity in cardiac arrest: Electrocardiographic presentations and management considerations based on the electrocardiogram,” *Am. J. Emerg. Med.*, 2012, doi: 10.1016/j.ajem.2010.08.017.

[21] V. Lionetti *et al.*, “Mismatch between uniform increase in cardiac glucose uptake and regional contractile dysfunction in pacing-induced heart failure,” *Am. J. Physiol. - Hear. Circ. Physiol.*, 2007, doi: 10.1152/ajpheart.00592.2007.

[22] A. Pingitore *et al.*, “Early subclinical increase in pulmonary water content in athletes performing sustained heavy exercise at sea level: Ultrasound lung comet-tail evidence,” *Am. J. Physiol. - Hear. Circ. Physiol.*, 2011, doi: 10.1152/ajpheart.00388.2011.

[23] P. Claus, A. M. S. Omar, G. Pedrizzetti, P. P. Sengupta, and E. Nagel, “Tissue Tracking Technology for Assessing Cardiac Mechanics: Principles, Normal Values, and Clinical Applications,” *JACC: Cardiovascular Imaging*. 2015, doi: 10.1016/j.jcmg.2015.11.001.

[24] T. S. Clemmensen, H. Eiskjær, B. B. Løgstrup, L. B. Ilkjær, and S. H. Poulsen, “Left ventricular global longitudinal strain predicts major adverse cardiac events and all-cause mortality in heart transplant patients,” *J. Hear. Lung Transplant.*, 2017, doi: 10.1016/j.healun.2016.12.002.

[25] L. Massari *et al.*, “A Machine-Learning-Based Approach to Solve Both Contact Location and Force in Soft Material Tactile Sensors,” *Soft Robot.*, 2020, doi: 10.1089/soro.2018.0172.

[26] D. Lo Presti *et al.*, “Fiber bragg gratings for medical applications and future challenges: A review,” *IEEE Access*, 2020, doi: 10.1109/ACCESS.2020.3019138.

[27] M. Granegger *et al.*, “Investigation of hemodynamics in the assisted isolated porcine heart,” *Int. J. Artif. Organs*, 2013, doi: 10.5301/ijao.5000257.

[28] S. Bai, J. Z. Kolter, and V. Koltun, “An empirical evaluation of generic convolutional and recurrent networks for sequence modeling,” *arXiv Prepr. arXiv1803.01271*, 2018.

[29] S. Hochreiter and J. Schmidhuber, “Long short-term memory,” *Neural Comput.*, vol. 9, no. 8, pp. 1735–1780, 1997.

[30] M. Suzgun, Y. Belinkov, S. Shieber, and S. Gehrmann, “LSTM Networks Can Perform Dynamic Counting,” 2019, doi: 10.18653/v1/w19-3905.

[31] G. P. Gravlee, S. D. Brauer, M. F. O’Rourke, and A. P. Avolio, “A comparison of brachial, femoral, and aortic intra-arterial pressures before and after cardiopulmonary bypass,” *Anaesth. Intensive Care*, 1989, doi: 10.1177/0310057x8901700311.

[32] J. Marquez, K. McCurry, D. A. Severyn, and M. R. Pinsky, “Ability of pulse power, esophageal Doppler, and arterial pulse pressure to estimate rapid changes in stroke volume in humans,” *Crit. Care Med.*, 2008, doi: 10.1097/CCM.0b013e31818b31f0.

[33] J. Zhang, L. A. H. Critchley, and L. Huang, “Five algorithms that calculate cardiac output from the arterial waveform: A comparison with Doppler ultrasound,” *Br. J. Anaesth.*, 2015, doi: 10.1093/bja/aev254.

[34] C. K. Ido *et al.*, “Hemodynamic variables in piglets anesthetized with isoflurane or propofol, kept under spontaneous ventilation and FIO2 of 0.5,” *Arq. Bras. Med. Vet. e Zootec.*, 2019, doi: 10.1590/1678-4162-10845.

[35] P. L. Wilkinson, J. R. Moyers, T. Ports, K. Chatterjee, D. Ullyott, and W. K. Hamilton, “Rate-pressure product and myocardial oxygen consumption during surgery for coronary artery bypass.,” *Circulation*, vol. 60, no. 2, pp. 170–173, 1979.

[36] C. Heelan, A. V. Nurmikko, and W. Truccolo, “FPGA implementation of deep-learning recurrent neural networks with sub-millisecond real-time latency for BCI-decoding of large-scale neural sensors (104 nodes),” in *Proceedings of the Annual International Conference of the IEEE Engineering in Medicine and Biology Society, EMBS*, 2018, doi: 10.1109/EMBC.2018.8512415.

[37] J. Redmon and A. Farhadi, “YOLO9000: better, faster, stronger,” in *Proceedings of the IEEE conference on computer vision and pattern recognition*, 2017, pp. 7263–7271.

[38] M. Perslev, M. H. Jensen, S. Darkner, P. J. Jennum, and C. Igel, “U-Time: A fully convolutional network for time series segmentation applied to sleep staging,” in *Advances in Neural Information Processing Systems*, 2019.

[39] P. C. Peng, J. H. Lin, H. Y. Tseng, and S. Chi, “Intensity and Wavelength-Division Multiplexing FBG Sensor System Using a Tunable Multiport Fiber Ring Laser,” *IEEE Photonics Technol. Lett.*, 2004, doi: 10.1109/LPT.2003.818916.

[40] C. E. Campanella, A. Cuccovillo, C. Campanella, A. Yurt, and V. M. N. Passaro, “Fibre Bragg Grating based strain sensors: Review of technology and applications,” *Sensors (Switzerland)*. 2018, doi: 10.3390/s18093115.

[41] A. Mazzoni *et al.*, “Morphological Neural Computation Restores Discrimination of Naturalistic Textures in Trans-radial Amputees,” *Sci. Rep.*, 2020, doi: 10.1038/s41598-020-57454-4.

[42] P. Saccomandi *et al.*, “Feedforward neural network for force coding of an MRI-compatible tactile sensor array based on fiber bragg grating,” *J. Sensors*, vol. 2015, pp. 1–9, 2015, doi: 10.1155/2015/367194.

[43] Y. E. Marin, T. Nannipieri, C. J. Oton, and F. DI Pasquale, “Current Status and Future Trends of Photonic-Integrated FBG Interrogators,” *J. Light. Technol.*, 2018, doi: 10.1109/JLT.2017.2779848.

[44] Y. E. Marin *et al.*, “Integrated Dynamic Wavelength Division Multiplexed FBG Sensor Interrogator on a Silicon Photonic Chip,” *J. Light. Technol.*, 2019, doi: 10.1109/JLT.2019.2919765.